JGR Atmospheres

RESEARCH ARTICLE

10.1029/2025JD045672

Holocene Hydroclimatic Variations Over Western and Central Asia as Inferred From Speleothem Isotope Evidence

Liang Ning[1], Fangmiao Xing[1], Zhengyu Liu[2], Jian Liu[1,3], Yanmin Qin[1], Qin Wen[1], Michael E. Mann[4], Yan Yu[5], Yongjin Wang[1], Mi Yan[1], Huayu Lu[6], Naixin Cao[1], Kefan Chen[1], and Weiyi Sun[1]

[1]State Key Laboratory of Climate System Prediction and Risk Management; Key Laboratory for Virtual Geographic Environment, Ministry of Education; State Key Laboratory Cultivation Base of Geographical Environment Evolution and regional response of Jiangsu Province; Jiangsu Center for Collaborative Innovation in Geographical Information Resource Development and Application; School of Geography, Nanjing Normal University, Nanjing, China, [2]Department of Geography, The Ohio State University, Columbus, OH, USA, [3]Jiangsu Provincial Key Laboratory for Numerical Simulation of Large Scale Complex Systems, School of Mathematical Science, Nanjing Normal University, Nanjing, China, [4]Department of Earth and Environmental Science, University of Pennsylvania, Philadelphia, PA, USA, [5]Department of Atmospheric and Oceanic Sciences, School of Physics, Peking University, Beijing, China, [6]School of Geography and Ocean Science, Nanjing University, Nanjing, China

Key Points:

- Enriching $\delta^{18}O_p$ trend over WA and ACA with precipitation decreases over WA and WCA but increases over ECA during the Holocene
- These $\delta^{18}O_p$ enrichments mainly result from decreases in precipitation weight from source regions
- These precipitation weight decreases are induced by precession-driven monsoon weakening and summer westerly strengthening

Supporting Information:

Supporting Information may be found in the online version of this article.

Correspondence to:

Z. Liu and J. Liu,
liu.7022@osu.edu;
jliu@njnu.edu.cn

Citation:

Ning, L., Xing, F., Liu, Z., Liu, J., Qin, Y., Wen, Q., et al. (2026). Holocene hydroclimatic variations over western and central Asia as inferred from speleothem isotope evidence. *Journal of Geophysical Research: Atmospheres*, *131*, e2025JD045672. https://doi.org/10.1029/2025JD045672

Received 18 OCT 2025
Accepted 18 FEB 2026

Author Contributions:

Conceptualization: Liang Ning
Data curation: Liang Ning, Fangmiao Xing, Yanmin Qin, Qin Wen
Formal analysis: Liang Ning, Fangmiao Xing, Zhengyu Liu, Yanmin Qin, Qin Wen
Funding acquisition: Jian Liu, Huayu Lu
Methodology: Yan Yu, Yongjin Wang
Supervision: Jian Liu
Visualization: Fangmiao Xing, Yanmin Qin
Writing – original draft: Liang Ning, Zhengyu Liu, Jian Liu, Yanmin Qin

Abstract

Recent studies have found a dipole pattern of hydroclimate variation in western Asia (WA) and arid central Asia (ACA) during the Holocene. However, speleothem $\delta^{18}O$ evidence shows some inconsistencies with other lines of evidence, especially concerning the timing of peak wetness in WA and precipitation trends in ACA. In an attempt to investigate these discrepancies, we employ the transient isotope-enabled simulation, that is, the iTraCE experiment, and water tagging sensitivity experiments driven by high and low precessions. The relationship between variations in water isotopes and precipitation and the underlying mechanisms are investigated. We find trends toward enriched $\delta^{18}O$ over three regions, with decreasing precipitation over WA and western central Asia (WCA) but increasing precipitation over eastern central Asia (ECA) during the Holocene. These opposing relationships between $\delta^{18}O$ and precipitation result from a number of different mechanisms. The $\delta^{18}O_p$ enrichments over WA, WCA, and ECA arise mainly from the Indian Ocean and Africa, North Atlantic Ocean, and Pacific Ocean source regions, respectively. These $\delta^{18}O_p$ enrichments result more from decreases of precipitation weight sourced from these regions than from increases of isotope ratio through the source and en route effects. These precipitation weight decreases and isotope ratio increases are tied to precession-driven changes in large-scale circulation, including the African monsoon weakening, winter polar front westerly jet weakening, summer subtropical westerly jet strengthening, and Asian monsoon weakening.

Plain Language Summary

Past studies have highlighted an apparent dipolar pattern of precipitation change in Asia during the Holocene epoch (the past 11,700 years), with drying in western Asia (WA) and wetting in the arid central Asia (ACA). Yet, one key line of evidence - speleothem $\delta^{18}O$—appears to contradict other climate records, creating confusion about how rainfall actually changed. Seeking to resolve this apparent contradiction, we used transient isotope-enabled simulation to track the movement of water molecules through the atmosphere over time. We found that while speleothem $\delta^{18}O$ becomes enriched across all regions though the Holocene, rainfall itself decreased in WA and WCA but increased in ECA. This seeming discrepancy arises from the fact that oxygen isotope levels don't just reflect total rainfall amounts but also moisture source regions. In this case, shifts in Earth's orbit altered large-scale wind patterns, weakening the winter polar front westerly jet and strengthening the summer subtropical westerly jet, altering the prevailing balance of different moisture source regions.

1. Introduction

Asian drylands, including arid central Asia (ACA; 36°−51°N, 53°−96°E) and western Asia (WA; 25°−41.5°N, 27°−53°E), with large populations and fragile ecosystems, are sensitive to climate changes. Although both ACA and WA are dominated by the westerlies, the precipitation variations show opposite trends in recent decades, with an increasing trend in ACA and a decreasing trend in WA (Chen et al., 2023). A similar dipole pattern of hydroclimate changes between ACA and WA was also found during the Holocene under the natural forcings (Chen et al., 2024; Ma et al., 2025). Based on multi-proxy analyses of loess-paleosol sequences, Chen et al. (2016)

Writing – review & editing: Liang Ning, Fangmiao Xing, Zhengyu Liu, Yanmin Qin, Qin Wen, Michael E. Mann, Yan Yu, Yongjin Wang, Mi Yan, Huayu Lu, Naixin Cao, Kefan Chen, Weiyi Sun

found a persistent wetting trend over ACA through the Holocene. This wetting trend is consistent with the pollen-based moisture records from lake sediments (Wang & Feng, 2013), stalagmite trace element ratios (Liu et al., 2020), and multiple types of moisture or precipitation records over the ACA (Chen et al., 2022).

Over the WA, based on a precisely dated record based on lipid biomarkers and water-level reconstruction from Almalou Peatland in the western Iranian Plateau, it is found that there is a drying trend toward the late Holocene (Chen et al., 2024). The Jeita Cave record in WA also shows two significant millennial scale drought periods during the middle to late Holocene (Cheng et al., 2015).

Actually, the ACA can be further divided into western CA (WCA; 36°–51°N, 53°–72°E) and eastern CA (ECA; 36°–51°N, 72°–96°E), which are dominated by cold season precipitation and warm season precipitation, respectively. Tan et al. (2024) found that there is a long-term drying trend in WCA, which is in contrast with the wetting trend in ECA, and these anti-phased precipitation changes result from different responses of winter and summer westerly jets to seasonal solar insolation over the past 8,000 years. This drying trend in the WCA is also supported by different types of records, such as reconstructions of sea level changes and salinity gradients in the Caspian Sea (Leroy et al., 2013, 2019).

For the mechanisms behind this dipole pattern, the intensity and position of westerlies due to the latitudinal insolation gradient play an important role in influencing water vapor transport (Chen et al., 2016). During the middle to late Holocene, strengthened westerlies induced increased precipitation in the ACA, and intensified subtropical high induced decreased precipitation in WA (Ma et al., 2025). Chen et al. (2024) found that the wetting trend during early Holocene (EH), a mid-Holocene (MH) hydroclimate optimum, and a rapidly drying trend during LH over WA are due to the pivotal shift of spring insolation.

Despite these progresses regarding the hydroclimate variations over WA and ACA, there are still some controversies, which result from discrepancies between isotope records and other proxy records. For example, over WA, the isotope records indicate that the wettest conditions occurred during the EH, while vegetation records indicate that the wettest conditions occurred during the MH (Ding et al., 2024). Over the ACA, enriching speleothem δ^{18}O records indicate a long-term drying trend if explained using the amount effect, which is opposite to other records; therefore, speleothem δ^{18}O records over the ACA should be affected more by the moisture source and water vapor transport pathways (Chen et al., 2022).

Therefore, the hydroclimate variations represented by the speleothem $\delta^{18}O_c$ records over the WA, WCA, and ECA need comprehensive investigations, because their climatic indications and corresponding mechanisms are unclear. The simulations based on the isotope-enabled Earth System Model provide an opportunity to clarify these issues and improve the understanding of hydroclimate changes during the Holocene. This will also help resolve the inconsistencies on hydroclimate variations represented by isotope records and other proxy records.

In this study, we used the transient isotope-enabled simulation through the Holocene, that is, iTraCE experiment, and a group of sensitivity experiments driven by high and low precessions to investigate the relationship between water isotope and precipitation over the WA, WCA, and ECA and the corresponding dominant mechanisms. Our results show that there are δ^{18}O enriching trends over the three regions, with decreasing precipitation over WA and WCA but increasing precipitation over ECA, consistent with previous studies. The consistent δ^{18}O enriching trends over the three regions are dominated by different mechanisms, resulting in these opposite relationships between δ^{18}O and precipitation.

2. Data and Methodologies

2.1. Proxy Reconstructions

The $\delta^{18}O_c$ records from 6 caves over the arid Asia region (Figure 1a) are used in this study, and their detailed information is shown in Table S1 of Supporting Information S1. There are three caves located at WA region, that is, Cave Jeita (Cheng et al., 2015), Cave Soreq (Orland et al., 2012), and Cave Sofular (Fleitmann et al., 2009), one cave at WCA region, that is, Cave Tonnelnaya (Cheng et al., 2016), and two caves at ECA region, that is, Cave Kesang (Cheng et al., 2016) and Cave Baluk (Liu et al., 2019). The speleothem data used are sourced from the NOAA/World Data Service for Paleoclimatology (https://www.ncei.noaa.gov/products/paleoclimatology/speleothem). In order to be consistent with the model data, the speleothem $\delta^{18}O_c$ records were uniformly averaged on a 50-year time slice. The moisture proxy records from 17 sites (Figure 1b) are also used to validate the simulated

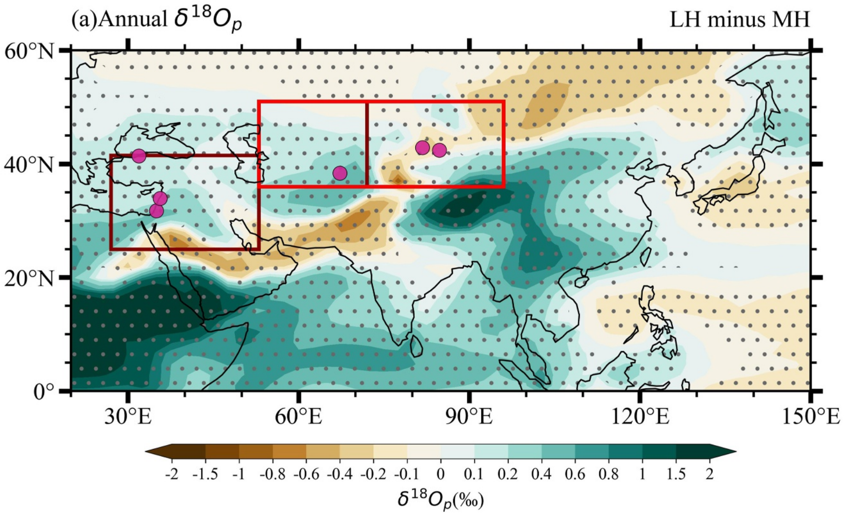

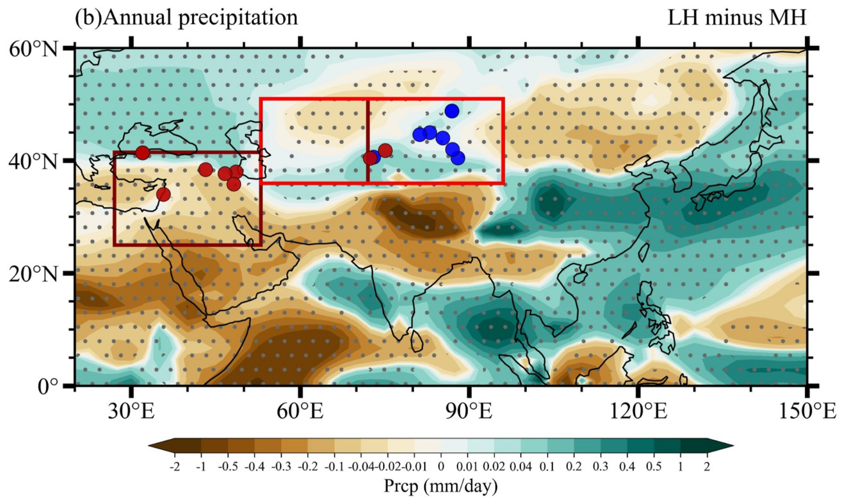

Figure 1. The changes of annual $\delta^{18}O_p$ (a, unit: ‰) and precipitation (b, unit: mm/day) between LH and MH simulated by the iTraCE experiment. The red dots in panel (a) are sites of six speleothem $\delta^{18}O_c$ records. The dots in panel (b) are sites of moisture proxy records, with blue indicating precipitation increases and red indicating precipitation decreases. The rectangles show West Asia, western Central Asia, and eastern Central Asia. Stippling indicates significant change at the 95% level based on a Student *t*-test. The detailed information of speleothem $\delta^{18}O_p$ records are listed in Table S1 of Supporting Information S1. The detailed information of moisture proxy records are listed in Table S2 of Supporting Information S1.

precipitation changes, and their detailed information are introduced in Table S2 of Supporting Information S1. Notably, nearly all the moisture proxy records are from ECA, with only the Talisman Cave drought index representing the hydroclimate variability in WCA although it locates the border between WCA and ECA (Tan et al., 2024).

2.2. iTraCE Experiment

The iTraCE experiment is the first set of transient simulations on global climate and water isotope ($\delta^{18}O_p$, δD) covering the period since the Last Glacial Maximum (LGM) (20ka-0ka BP) using the isotope-enabled Community Earth System Model version 1.3 (iCESM1.3). Following the experimental design of its precursor TraCE (Liu et al., 2009), the iTraCE Holocene simulation is driven by four external forcings (ICE + ORB + GHG + MWF), that is, the ice sheet and ocean bathymetry (ICE), orbital parameters (ORB), greenhouse gas concentrations (GHG), and meltwater fluxes (MWF) (He et al., 2021a).

The iTraCE simulation for the Last Deglaciation (LD) (20 ka–11 ka BP) has been analyzed regarding the hydroclimate footprint of Asian monsoon water isotopes (He et al., 2021a), and the South China hydroclimate variability dominated by autumn rainfall (He et al., 2021b). The iTraCE simulation for the Holocene was branched from the iTraCE Last Deglaciation simulation at 11 ka BP. During the Holocene, the iTraCE simulation captures the major climatological features of observed hydroclimate variables in the Asian monsoon region (Ning, Liu, et al., 2025). The simulated climatology and seasonal variations of $\delta^{18}O_p$ are close to the observations at six GNIP stations (Figure S1 in Supporting Information S1) with detailed information listed in Table S3 of Supporting Information S1. This transient simulation provides a unique opportunity for comprehensive data-model comparisons between $\delta^{18}O$ and associated hydroclimate changes over the arid Asia region during the Holocene (Figure 1).

2.3. Tagging Experiments

To explain the mechanisms behind the $\delta^{18}O_p$ changes, and their relationship with precipitation changes, two water vapor tagging sensitivity experiments are performed. Similar tagging experiments have been widely used to track sources and analyze corresponding mechanisms of moisture changes over specific regions in previous studies (e.g., Man et al., 2022). Given that the Holocene climate was primarily driven by precession—i.e., changes in the seasonal distribution of solar insolation—two sets of sensitivity experiments were performed using iCESM, that is, one with high precession (P_{max}, denoting precession during LH) and the other with low precession (P_{min}, denoting precession during MH). To maximize the hydroclimatic response to insolation forcing, the P_{min} and P_{max} configurations were selected to closely align with the periods of 127 ka and 116 ka, rather than strictly adhering to the LH and MH timeframes.

The P_{min} and P_{max} tagging experiments are established in the atmospheric component model iCAM5.3 with the forcings of sea ice distribution, sea surface temperature, sea surface $\delta^{18}O$ and δD from our previously 150,000-year transient simulation (Wen et al., 2024), and the orbital parameters are set at the P_{min} and P_{max} periods, respectively. Each tagging experiment is integrated for 40 years with the last 20 years used to analyzed. The difference of P_{max} and P_{min} ($P_{max} - P_{min}$) well reproduces hydrological climate change from middle to late Holocene (LH) in iTraCE simulation (Figure S2 in Supporting Information S1).

In the tagging experiments, there are 25 tagging subregions divided from the globally horizontal range, with 13 regions covering the ocean and 12 regions covering the land. Hence, the life cycles of $H_2{}^{16}O$ (vapor) and $H_2{}^{18}O$ are tracked from each tagging region (source region) to the sink region, transited by atmospheric circulation and hydrological processes, that is, evaporation and rainout. In this study, to investigate the moisture sources over WA, WCA, and ECA, these 25 regions are grouped into seven regions: North Atlantic Ocean (ocean, 10°N−70°N; 0°−100°W), the Indian Ocean (ocean, 40°S−30°N; 20°E−100°E), the Pacific Ocean (ocean, 40°S−70°N; 100°E−70°W), Europe (land, 35°N−90°N; 0°−60°E), Africa (land, 60°S−35°N; 0°−60°E), Center Asia (land, 25°N−90°N; 60°E−105°E), and the rest of the globe, which is denoted as the "other" region (ocean and land). Thus, the precipitation P ($H_2{}^{16}O$) and $\delta^{18}O$ of precipitation ($\delta^{18}O_p$) at a grid point are equivalent to the sum of the seven tagging (source) regions ($i = 1, 2, 3, \ldots, 7$):

$$P = \sum_{i=1}^{7} P_i, \delta^{18}O_p = \sum_{i=1}^{7} \delta^{18}O_i \left(\frac{P_i}{P}\right) \tag{1}$$

where P_i and $\delta^{18}O_i$ represent the precipitation and $\delta^{18}O$ from the source regions "i."

2.4. Decomposition of $\delta^{18}O_p$ Changes

There are two steps of the decomposition for the $\delta^{18}O_p$ change at a grid point. In the first step, the change of $\delta^{18}O_p$ from the P_{min} to P_{max} period, $\Delta\delta^{18}O_p = \delta^{18}O_{p,P\,max} - \delta^{18}O_{p,P\,min}$, can be decomposed into two parts: the isotope ratio $\Delta\delta^{18}O_p$ change and precipitation weight $\Delta\left(\frac{P_i}{P}\right)$ change from the source region:

$$\Delta\delta^{18}O_p = \sum_{i=1}^{7} \left(\frac{P_i}{P}\right) \cdot \Delta\delta^{18}O_{pi} + \sum_{i=1}^{7} \delta^{18}O_{pi} \cdot \Delta\left(\frac{P_i}{P}\right) \tag{2}$$

In the second step, the isotope ratio $\Delta\delta^{18}O_p$ change can continue to be decomposed into three parts according to its life cycle along the trajectory from the source region to the sink region:

$$\Delta\delta^{18}\mathrm{O}_{pi} = \Delta\left(\delta^{18}\mathrm{O}_{v,\mathrm{source},i}\right) + \Delta\left(\delta^{18}\mathrm{O}_{v,\mathrm{sink},i} - \delta^{18}\mathrm{O}_{v,\mathrm{source},i}\right) + \Delta\left(\Delta\delta^{18}\mathrm{O}_{pi} - \delta^{18}\mathrm{O}_{v,\mathrm{sink},i}\right) \quad (3)$$

On the right-hand side, the first term is the change of the vapor δ^{18}O ($\delta^{18}O_v$) in the source region, which is generated by the net effect of local precipitation and evaporation in the source region. The second term is the change of the $\delta^{18}O_v$ due to the en route depletion, which associated with the rainout along its trajectory from the source region to the sink region. The third term describes the transition from vapor $\delta^{18}O_v$ to the precipitation $\delta^{18}O_p$, representing the change of local condensation enrichment.

3. Results

3.1. $\delta^{18}O_p$ and Hydroclimate Variations Through Holocene

Figure 1 shows simulated changes of annual $\delta^{18}O_p$ and precipitation between LH and MH by the iTraCE experiment. There are $\delta^{18}O_p$ enrichments over the whole Eurasia, except a belt region from northeastern Asia through eastern Central Asia to southern West Asia. This belt divides the $\delta^{18}O_p$ enrichment region into two parts, which are dominated by summer $\delta^{18}O_p$ enrichment and the other three seasons' $\delta^{18}O_p$ enrichments, respectively (Figure S3 in Supporting Information S1). These two regions with $\delta^{18}O_p$ enrichment correspond to the regions dominated by summer precipitation (ECA) and winter precipitation (WA and WCA; Tan et al., 2024). This sandwich pattern of $\delta^{18}O_p$ changes is mainly caused by changes in summer and autumn, which show a dipole pattern between the monsoon and arid regions and a similar sandwich pattern, respectively (Figure S3 in Supporting Information S1). The changes in spring and winter show uniform enrichments over the whole Eurasia (Figure S3 in Supporting Information S1). Thus, the observed $\delta^{18}O_c$ enrichments in WA and WCA are due to changes in spring, autumn, and winter. While, the observed $\delta^{18}O_c$ enrichments in ECA are also due to changes in spring, autumn, and winter. However, this cannot rule out the contributions from summer $\delta^{18}O_p$ changes, because ECA just lies on the belt. Therefore, whether summer $\delta^{18}O_p$ enrichments over the monsoon region also contribute to the observed $\delta^{18}O_c$ enrichment in ECA is really related to the precision of the iTraCE simulation on reproducing the monsoon extension. This issue may be investigated systemically in further studies. Another issue is that these seasonal $\delta^{18}O_p$ changes are not weighted by precipitation, so their relative contributions to the annual $\delta^{18}O_p$ changes are related to the ratios of their precipitation to the annual precipitation.

For the annual precipitation changes, there are precipitation decreases over northeastern China, through southwestern China and South Asia to northern Africa, and precipitation increases over middle eastern China and western Central Asia, consistent with most moisture proxy records (Figure 1b). The seasonal precipitation changes also show that the pattern of annual precipitation changes is more similar to the summer precipitation changes, with precipitation decreases over northeastern China through southwestern China and South Asia to northern Africa (Figure S4 in Supporting Information S1). In spring, there precipitation increases over East Asia and Central Asia but decreases over West Asia and South Asia. In autumn, there are only precipitation increases over southern China and Southeast Asia, and precipitation decreases over other regions. In winter, there are precipitation increases over most regions. Thus, the precipitation decreases over WA are due to precipitation decreases in spring, summer, and winter. The precipitation decreases over WCA are due to precipitation decreases in summer, autumn, and winter. The precipitation increases over the ECA are due to precipitation increases in spring, summer, and winter.

The regional mean annual precipitation weighted $\delta^{18}O_p$ changes show enrichments over the three regions (Figure 3), consistent with observed speleothem $\delta^{18}O_c$ changes (Figure 2a). The regional precipitation changes show precipitation decreases over WA and WCA, but precipitation increases over ECA, consistent with moisture proxy records (Figures 2c and 2d) in previous studies (e.g., Tan et al., 2024). However, soil moisture decreases and temperature increases over all three regions (Figure 3). Notably, this early Holocene peak timing of simulated precipitation over WA is different from the middle Holocene peak timing of several hydroclimate reconstructions based on vegetation and peatland indicators (Figure 2). This delayed ecosystem response to precipitation peak may be caused by the vegetation response to winter warming and the subsequent feedback with soil moisture, as found in previous studies (Cheng et al., 2021). Furthermore, other reasons, such as the lack of dynamic vegetation in iTraCE and uncertainty of proxy records' climate interpretation, may also contribute to this mismatch of peak timings.

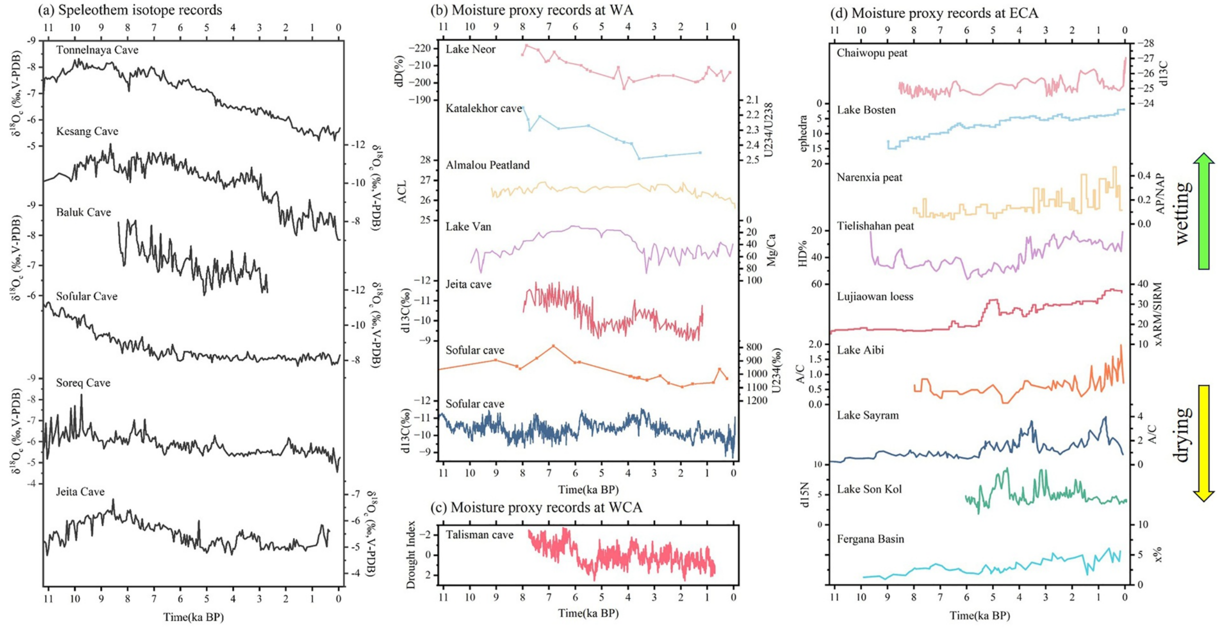

Figure 2. Time series of speleothem $\delta^{18}O_c$ records (unit: ‰) at six caves (a) and 17 moisture proxy records (b–d) over three regions.

3.2. Decomposition of $\delta^{18}O_p$ and Precipitation Changes Based on Tagging Experiments

To explain the mechanisms behind the $\delta^{18}O_p$ changes and their relationship with precipitation changes, the results from two water vapor tagging experiments are compared. Because the timing choices of 127 ka (P_{min}) and 116 ka (P_{max}) in the tagging experiments are not strictly MH and LH, these magnitudes of precipitation and isotope changes may be a little bit different from the iTraCE results. The seasonal variations of $\delta^{18}O_p$, precipitation amount, and precipitation weights from different source regions at low and high precession conditions are first shown in Figures S5 and S6 of Supporting Information S1, respectively. Over three regions, under both conditions, the seasonal cycles of $\delta^{18}O_p$ are dominated by moisture from the northern Atlantic, followed by little contribution from others over WA and WCA, and central Asia and Pacific during summer over ECA (Figures S5a–S5c and S6a–S6c in Supporting Information S1). This is consistent with winter and spring precipitation mainly from the northern Atlantic over WA and WCA (Figures S5d, S5e, S5g, S5h, and S6d, S6e, S6g, S6h in Supporting Information S1). Over ECA, the summer precipitation is contributed mostly from central Asia,

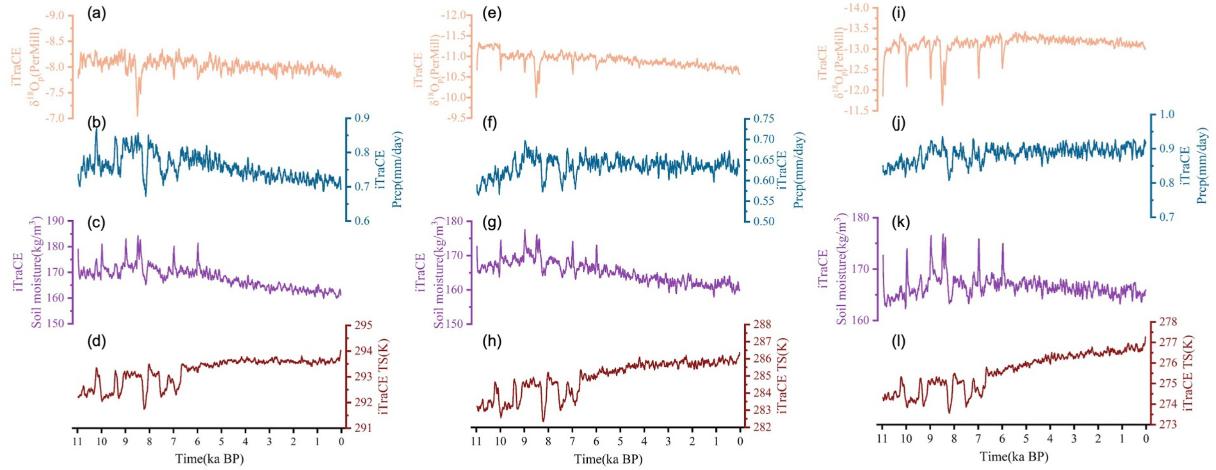

Figure 3. Simulated annual $\delta^{18}O_p$ (a, e, i; unit: ‰), precipitation (b, f, j; unit: mm/day), soil moisture (c, g, k; unit: kg/m^3), and surface temperature (d, h, l; unit: K) over WA (a–d), WCA (e–h), and ECA (i–l) through the Holocene by iTraCE experiment.

followed by winter and spring precipitation mainly from the northern Atlantic (Figures S5f, S5i and Figures S6f, S6i in Supporting Information S1).

Local annual $\delta^{18}O_p$ changes originated remotely from each source region are shown in Figure 4. Quantitatively, WA, WCA, and ECA exhibit overall enriched $\delta^{18}O_p$ from low precession to high precession (Figures 4v–4x), which are consistent with both simulated and observed time series of $\delta^{18}O$ within these three regions (Figure 3). In both P_{max} and P_{min} experiments, climatological $\delta^{18}O_p$ over three regions is mainly from remote sources, that is, the North Atlantic (Figures 4a and 4h), and $\delta^{18}O_p$ over ECA is also from adjacent regions, that is, south of central Asia (Figures 4f and 4m) and the Pacific Ocean (Figures 4c and 4j), consistent with the results of seasonal cycles (Figures S5a–S5c and S6a–S6c in Supporting Information S1). The differences between P_{max} (LH) and P_{min} (MH) show that, the $\delta^{18}O_p$ enrichments over WA are mainly from the Indian Ocean (Figure 4p) and Africa (Figure 4s) although these two regions only contribute about 10%–20% of precipitation over WA (Figure S5g in Supporting Information S1), and $\delta^{18}O_p$ enrichments over WCA are mainly from the North Atlantic Ocean (Figure 4o). In ECA, the $\delta^{18}O_p$ changes should be divided into two parts, the $\delta^{18}O_p$ enrichments mainly originate from the Pacific Ocean (Figure 4q), while the $\delta^{18}O_p$ depletion mainly originate from the North Atlantic Ocean (Figure 4o) and Europe (Figure 4r). Interestingly, the $\delta^{18}O_p$ from Pacific Ocean induces $\delta^{18}O_p$ enrichments over both WCA and ECA (Figure 4q), although the Pacific Ocean only contributes less than 10% of precipitation over WCA and ECA (Figures S5h and S5i in Supporting Information S1). In contrast, the $\delta^{18}O_p$ from North Atlantic Ocean causes $\delta^{18}O_p$ enrichment over WCA but depletion over the ECA (Figure 4o).

Then, as explained in Section 2.4, the change of $\delta^{18}O_p$ are decomposed into changes due to precipitation weight $\Delta\left(\frac{P_i}{P}\right)$ change and isotope ratio $\Delta\delta^{18}O_p$ change from the source region. Notably, the precipitation weight change is not equal to the absolute precipitation amount change. For example, a decrease in precipitation weight from a source may indicate either an absolute decrease in precipitation from that source or a relatively smaller precipitation increase compared with other sources. The results show that enriched $\delta^{18}O_p$ values over WA and ACA are more due to the precipitation weight changes, than the changes in the isotope ratio $\Delta\delta^{18}O_p$ (Figure 5), indicating that the local $\delta^{18}O_p$ changes more associated with the precipitation weight changes from the source region, similar to the East Asian monsoon region (Jing et al., 2025). Detailly, the $\delta^{18}O_p$ enrichments over WA originated from tropics, that is, Indian Ocean and Africa (Figures 5b and 5e), are due to the decreased precipitation weights from these two regions (Figures S7b and S7e in Supporting Information S1). This relationship between enrichment of local $\delta^{18}O_p$ associated with the decreased precipitation weight change from source region at orbital time scale (Figures S7b and S7e in Supporting Information S1), is because the $\delta^{18}O_{pi}$ in Equation 2 is negative. The $\delta^{18}O_p$ enrichments over WCA (Figure 5a) are caused by the decreased precipitation weight from the North Atlantic (Figure S7a in Supporting Information S1), in which boreal winter (DJF) precipitation weight change makes a larger contribution (Figure S9a in Supporting Information S1). The $\delta^{18}O_p$ enrichments over ECA (Figure 5c) are due to the decreased precipitation weight from the Pacific Ocean (Figure S7c in Supporting Information S1), while the $\delta^{18}O_p$ depletions are related to the summer (JJA) precipitation weight increases over the North Atlantic Ocean and Europe (Figures 5a, 5d and Figures S10a, S10d in Supporting Information S1). The regional mean contributions from seven moisture source regions (Figures 5o–5q) also confirm that, the $\delta^{18}O_p$ enrichment over WA from Indian Ocean and Africa, the $\delta^{18}O_p$ enrichment over WCA from North Atlantic Ocean, and the $\delta^{18}O_p$ enrichment over ECA from Pacific Ocean. These results emphasize that different seasons dominate $\delta^{18}O_p$ changes over WA, WCA, and ECA, posing a potential boundary of annual $\delta^{18}O_p$ changes between WCA and ECA. Moreover, these significant $\delta^{18}O_p$ changes from MH to LH directly caused by remote precipitation weight changes imply a shift of the moisture source, although the roles of the North Atlantic Ocean and central Asia as dominant moisture sources do not change (Figures S5 and S6in Supporting Information S1).

The precipitation amount and precipitation weight changes from seven moisture source regions are shown in Figures S7 of Supporting Information S1, with regional mean results summarized in Figures S7o–S7t of Supporting Information S1. These decreased precipitation weights from the Indian Ocean and Africa over WA (Figures S7b and S7e in Supporting Information S1) are associated with decreased precipitation amounts (Figures S7i and S7k in Supporting Information S1), especially for summer (Figures S8i and S8k in Supporting Information S1) and winter (Figures S9i and S9k in Supporting Information S1). Notably, there are increased precipitation amounts and precipitation weights locating south of WA from the Indian Ocean (Figure S7i in Supporting Information S1), resulting in increased regional mean precipitation amounts and precipitation weights (Figure S7o in Supporting Information S1), although there are decreased precipitation amounts and precipitation

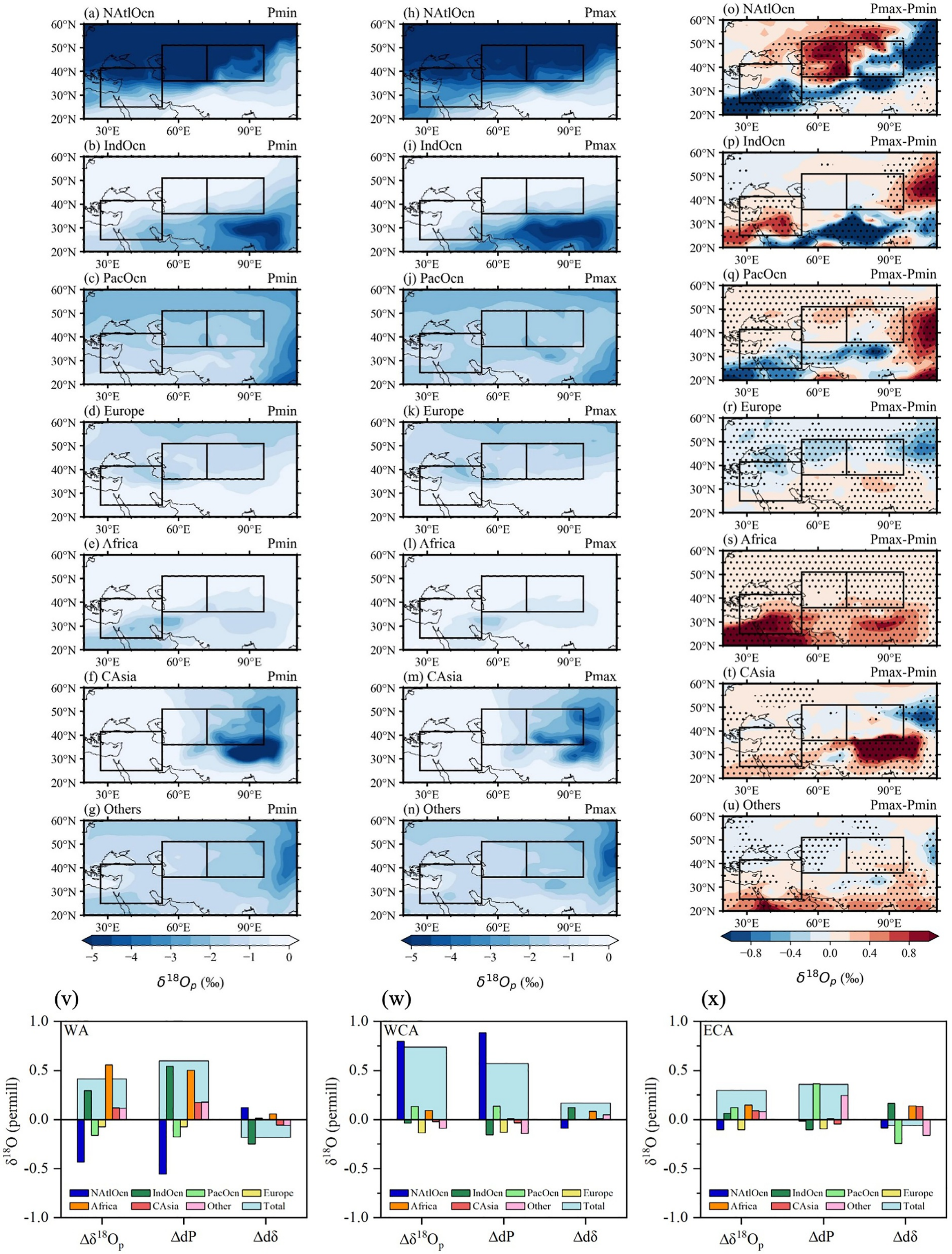

Figure 4. The simulated climatology of $\delta^{18}O_p$ from northern Atlantic, Indian Ocean, Pacific Ocean, Europe, Africa, Central Asia, and others at low precession (a–g; unit: ‰), high precession (h–n; unit: ‰), differences between high precession and low precession (o–u; unit: ‰), and regional averages over West Asia (v; unit: ‰), West Central Asia (w; unit: ‰), and East Central Asia (x; unit: ‰) based on sensitivity experiments.

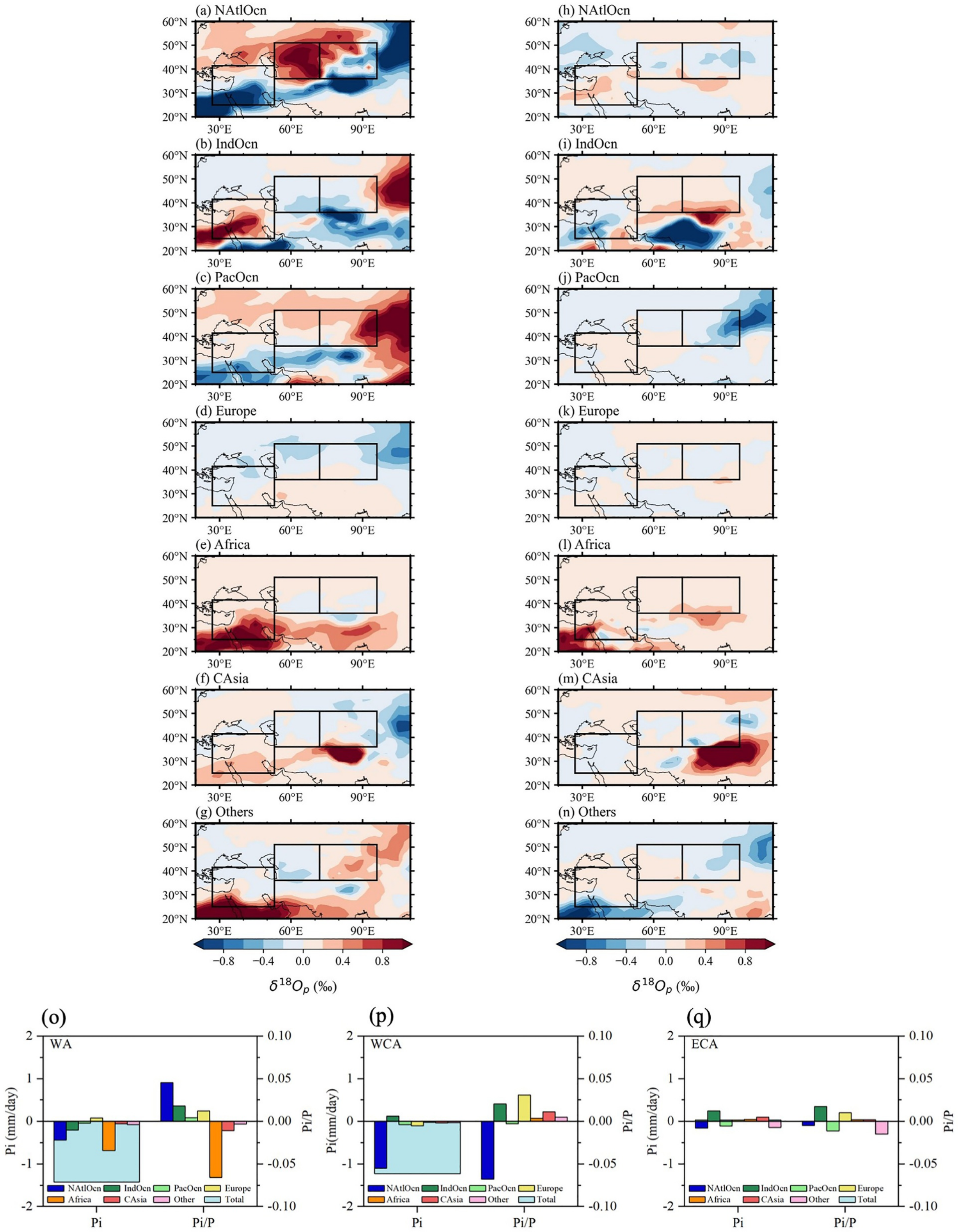

Figure 5. The simulated $\delta^{18}O_p$ differences between high precession and low precession from northern Atlantic, Indian Ocean, Pacific Ocean, Europe, Africa, Central Asia, and others due to precipitation weight changes (a–g; unit: ‰) and $\delta^{18}O_p$ changes (h–n; unit: ‰), corresponding regional mean contributions from seven moisture source regions over three regions (o–q; unit: ‰) based on sensitivity experiments.

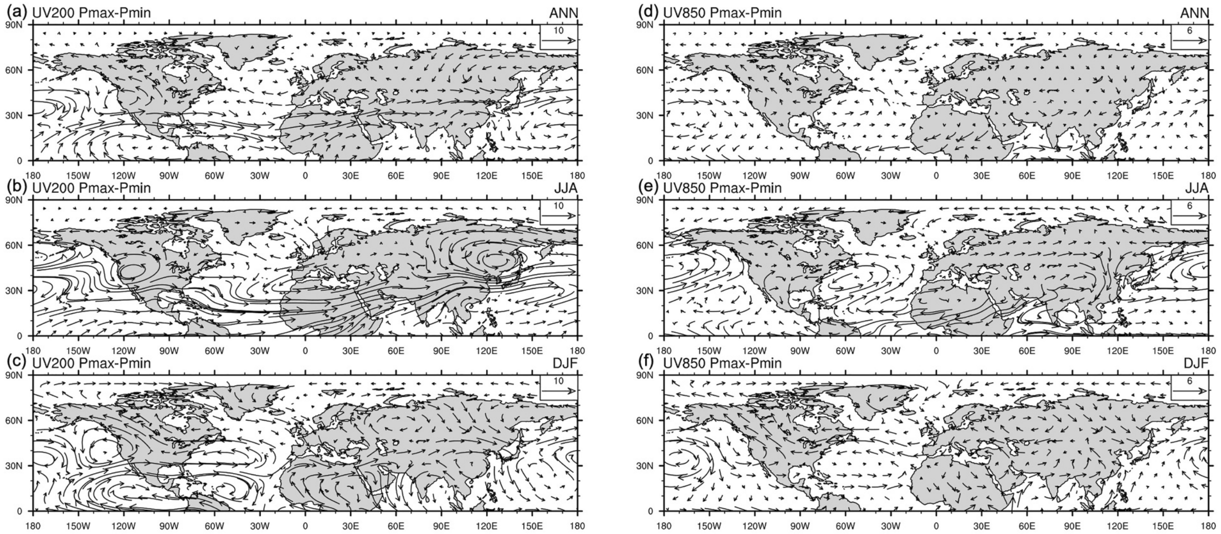

Figure 6. The simulated annual (a, d), JJA (b, e), and DJF (c, f) 200 hPa (a–c) and 850 hPa (d–f) wind differences (unit: m/s) between high precession and low precession based on sensitivity experiments.

weights over most of WA (Figure S7i in Supporting Information S1). The decreased precipitation weight from the North Atlantic over the WCA (Figure S7a in Supporting Information S1) is associated with decreased precipitation amounts (Figure S6h in Supporting Information S1), especially for winter (Figure S9h in Supporting Information S1). The decreased precipitation weight from Pacific over ECA (Figure S7c in Supporting Information S1) is associated with decreased precipitation amounts (Figure S7j in Supporting Information S1), especially for summer (Figure S8j in Supporting Information S1). The magnitudes of these changes over ECA (Figure S7t in Supporting Information S1) are smaller than those changes over WA and WCA (Figures S7o and S7p in Supporting Information S1).

For the part of $\delta^{18}O_p$ change due to isotope ratio ($\Delta\delta^{18}O$), WA $\delta^{18}O_p$ enrichments are associated with isotope ratio changes from the North Atlantic Ocean and Africa (Figures 5h and 5l). On one hand, the moisture containing enriched $\delta^{18}O_p$ could be transported from the North Atlantic Ocean (Figure S9a in Supporting Information S1) with less rainout along its trajectory in P_{max} (Figure S10h in Supporting Information S1). The $\delta^{18}O_p$ enrichment of the source region term is caused by reduced precipitation over the North Atlantic Ocean (Figures S2a and S2c in Supporting Information S1). The $\delta^{18}O_p$ enrichment of the en route term is caused by reduced precipitation along the trajectory due to winter polar front westerly jet weakening. On the other hand, moisture containing $\delta^{18}O_p$ from North Africa also contribute to $\delta^{18}O_p$ enrichment over the southwest of WA through source term (Figure S9e in Supporting Information S1) and reduced local condensation (Figure S10s in Supporting Information S1).

Similarly, WCA and ECA $\delta^{18}O_p$ enrichments result from moisture with enriched $\delta^{18}O_p$ sourcing from Indian Ocean and Africa (Figures 5i and 5l) through the source and en route effects (Figures S10b, S10e, S10i, and S10l in Supporting Information S1), indicating less precipitation over these two source regions and along their trajectory in P_{max}. This suggests overall weakening of African monsoon and Indian monsoon in P_{max} (during the LH, Figure 6d). This is consistent with African summer monsoon weakening and southward retreat due to the reduced summer solar insolation through the Holocene opposite to the Late Interglacial period (Orland et al., 2019). This African monsoon weakening was also accompanied by a southward shift of tropical rainfall (Figure S11 in Supporting Information S1).

3.3. Mechanisms Behind the $\delta^{18}O_p$ Changes

With changes in large-scale atmospheric circulations, we further explore the relevant mechanisms behind $\delta^{18}O_p$ changes due to precipitation weight changes and isotope ratio changes from MH (P_{min}) to LH (P_{max}). The simulated 200 hPa and 850 hPa wind differences between P_{max} and P_{min} show that, in boreal winter (DJF) season, weaker polar front westerly jet (Figure 6c) combined with reduced precipitation weight and amount from North Atlantic Ocean in P_{max} (Figures S7a and S7h in Supporting Information S1) results $\delta^{18}O_p$ enrichment over WCA and northwestern ECA (Figure 5a). This reduced winter precipitation over WCA and WA (Figure S2c in Supporting Information S1) are consistent with the proxy records in Tan et al. (2024) (Figure 2). The 200 hPa eddy kinetic energy changes also confirm this winter polar front westerly jet weakening (Figure S12 in Supporting Information S1), with corresponding reduced moisture transport (Figure S13 in Supporting Information S1). Northeastern wind anomalies associated with weakened African monsoon due to the reduced insolation and land-sea thermal contrast (Figures 5d and 5e) resulted reduced precipitation weight and amount from Indian Ocean and Africa in $P_{\max}$ (Figures S7b, S7e, S7i, and S7l in Supporting Information S1) and corresponding $\delta^{18}O_p$ enrichment over WA (Figures 5b and 5e), mainly for the summer (Figures S8b, S8e, S8i, and S8j in Supporting Information S1) rather than winter (Figures S9b, S9e, S9i, and S9j in Supporting Information S1), consistent with previous studies (e.g., Chen et al., 2024). On the other aspect, in boreal summer season (JJA), the enhanced summer subtropical westerly jet (Figure 6b and Figure S14 in Supporting Information S1) overlaid with the weakened East Asia monsoon (Figure 6e) causes the $\delta^{18}O_p$ enrichments over ECA (Figure 5c) through reduced precipitation weight and amount from the Pacific (Figures S7c, S7j and S8c, S8j in Supporting Information S1) due to the reduced moisture transport (Figure S15 in Supporting Information S1). This influence from the Pacific on ECA is weaker with smaller $\delta^{18}O_p$ and precipitation changes compared with those influences over WA and WCA.

Notably, a weaker polar front westerly jet induces reduced precipitation weight from the North Atlantic Ocean over WA and ACA during winter (Figure S9a in Supporting Information S1), but this effect is compensated by increased precipitation weight during summer (Figure S8a in Supporting Information S1), resulting only in reduced precipitation weight and $\delta^{18}O_p$ enrichment over WCA and northwestern ECA from the North Atlantic Ocean on an annual scale (Figures 5b and 5c). Similarly, the reduced precipitation weight from the Indian Ocean over ACA during summer (Figure S8b in Supporting Information S1) is compensated by increased precipitation weight during winter (Figure S9b in Supporting Information S1), resulting in only reduced precipitation weight and $\delta^{18}O_p$ enrichment over WA from the Indian Ocean on an annual scale (Figure 5a).

The $\delta^{18}O_p$ enrichments of the source region term caused by reduced precipitation over the North Atlantic Ocean to WA (Figures S2a and S2c in Supporting Information S1) are related to the anti-cyclonic circulation at eastern North Atlantic (Figures 6d–6f). The $\delta^{18}O_p$ enrichments of source region terms caused by reduced precipitation over the Indian Ocean and Africa to WCA and ECA (Figures S2a and S2b in Supporting Information S1) are related to the weakening of African monsoon and Indian monsoon (Figures 6d and 6e). Moreover, moisture with enriched $\delta^{18}O_p$ transported from the North Atlantic Ocean is also dominated by the northward polar front westerly jet in winter, resulting the $\delta^{18}O_p$ enrichments over WA through the en route effect due to reduced precipitation along the trajectory (Figure S2a in Supporting Information S1). Moisture with enriched $\delta^{18}O_p$ transported from the tropical Indian Ocean and Africa is also dominated by reduced precipitation along the trajectory (Figure S2a in Supporting Information S1), resulting the $\delta^{18}O_p$ enrichments over WCA and ECA through the en route effect.

The isotope changes from the North Atlantic due to moisture trajectory changes discussed in previous studies (e.g., Tan et al., 2024) are further examined through the change of 850 hPa eddy kinetic energy. The results show that the eddy kinetic energy decreases over the Mediterranean Sea during the $P_{\max}$ period (Figure S16 in Supporting Information S1), indicating reduced storms. This confirms the northward shift of the winter polar front westerly jet and reduced Mediterranean storm activity, which decreases the moisture transfer and winter precipitation in the WCA (Tan et al., 2024).

4. Discussions

For the model simulations, differences between observed and simulated monsoon margins may impact the conclusion. For example, the previous studies (Chen et al., 2022) indicate the $\delta^{18}O_p$ source shift from the Indian Ocean to the Pacific Ocean due to the monsoon weakening; however, this enhanced $\delta^{18}O_p$ from Pacific Ocean is not obvious, because the model simulated influence locates more eastward than in the observation (Figure 4q). This also implies when comparing simulations and reconstructions, regional mean rather than single grid point from simulations should be compared with each single point from proxy records, if each proxy record represents some regional scale climate rather than local climate. Furthermore, simulations show that ACA is located in a region influenced by monsoon and westerly, resulting in complicated water resources (Chen et al., 2022), which may induce a discrepancy among the proxy records. Meanwhile, current results based on the iTraCE experiment relies on only one member of a single model, so the potential influences due to model dependence and internal variability should be excluded in further studies using more ensemble members from multiple models.

For $\delta^{18}O_p$ decompositions, the relative contributions from values of precipitation weight $\Delta\left(\frac{p_i}{p}\right)$ are usually larger than the value of isotope ratio $\Delta\delta^{18}O_p$. This is potentially because the climatological precipitation amounts are small, about 300 mm in observation. So the $\delta^{18}O_p$ changes are more sensitive to the precipitation weights, which are usually considered as changes of $\delta^{18}O_p$ source regions. However, this $\delta^{18}O_p$ changes may result from some moisture source regions that are not dominant moisture source regions. For example, the $\delta^{18}O_p$ enrichment over ECA due to decreased precipitation sourcing from the Pacific Ocean (Figure 5c), the mechanism is not straightforward because the Pacific Ocean is not a typical moisture source to ECA and contributes only less than 10% of total precipitation (Figures S5i and S6i in Supporting Information S1). This is because the $\delta^{18}O_p$ and precipitation changes over ECA are small, slight precipitation weight decrease from the Pacific Ocean of ~5% (Figure S7q in Supporting Information S1) is more obvious than other regions. Comparisons of precipitation amount and precipitation weight between low (Figures S5f and S5i in Supporting Information S1) and high precession conditions (Figures S6f and S6i in Supporting Information S1) show that low precipitation climatology from the Pacific Ocean amplifies the influence of this slight summer weight decrease, when the precipitation weights from other dominant moisture pathways are almost unchanged. This also indicates the high sensitivity of hydroclimate over ECA. Therefore, future investigation of $\delta^{18}O_p$ changes should not ignore untypical moisture source regions.

Furthermore, the magnitudes of simulated $\delta^{18}O_p$ changes (~1‰) are smaller than those magnitudes of reconstructed $\delta^{18}O_p$ changes (~2‰), indicating the weaker model responses to orbital forcings. Potential reasons for this systematic underestimation include simplified cloud microphysics and convection parameterization schemes, weak coupling of dynamic processes and fractionation, missing isotope cycling processes, coarse resolution and insufficient description of complex terrain. The relative contributions of terms dominating the $\delta^{18}O$ changes in response to orbital forcings in the current study may be biased. This underestimation may also pose challenges to direct comparison between simulation and reconstruction, and further applications of the simulated results, such as data assimilation, therefore bias corrections may be needed before the applications.

Another potential limitation of the current study is that the tagging sensitivity experiment was driven orbital parameters of 127 ka and 116 ka rather than exact forcings of mid- and late Holocene. The differences in experimental designs may impact the conclusions since the isotope transport is sensitive to the background climate states. Therefore, to fully quantify the contribution of the precipitation weight mechanism in the Holocene isotope changes, we think a group of tagging sensitivity experiments driven by exact forcings of the middle and late Holocene should be performed in the future studies.

5. Conclusions

In this study, oxygen isotope and precipitation changes over the WA, WCA, and ECA during the Holocene, and corresponding mechanisms were investigated through the iTraCE experiments and a group of sensitivity experiments driven by high and low precession. These experiments capture the detailed influences on oxygen isotopic fractionation as moisture is transported by large-scale atmospheric circulation.

The iTraCE transient simulation produce $\delta^{18}O$ enrichment trends during the course of the Holocene over the three regions, with decreasing precipitation over WA and WCA but increasing precipitation over ECA, consistent with a wealth of evidence from previous studies. The mechanisms behind these opposing relationships between $\delta^{18}O$ and precipitation in different regions were investigated by decomposing $\delta^{18}O_p$ changes into various contributions using a series of sensitivity experiments. The $\delta^{18}O_p$ changes from P_{min} to P_{max} were decomposed into components associated with changes in precipitation weight and isotope ratios from different source regions.

The consistent $\delta^{18}O$ enriching trends over the three regions are dominated by different mechanisms, resulting in these opposite relationships between $\delta^{18}O$ and precipitation. The $\delta^{18}O_p$ enrichments over WA, WCA, and ECA are mainly tied to decreased moisture contributions from the Indian Ocean and Africa, the North Atlantic Ocean, and the Pacific Ocean, respectively. Those changes, in turn, are tied to African summer monsoon weakening, weakened winter westerlies and strengthened summer westerlies as well as the weakening of the East Asian summer monsoon (EASM). These mechanisms are shown in the schematic diagrams (Figure 7). The magnitudes of $\delta^{18}O$ and precipitation changes over WA and WCA are far greater than those over ECA. Notably, when investigating the changes in different seasons, the source regions dominating changes of $\delta^{18}O$ and precipitation weight in the whole year may not be the typical source regions in climatology, due to the compensations among different seasons.

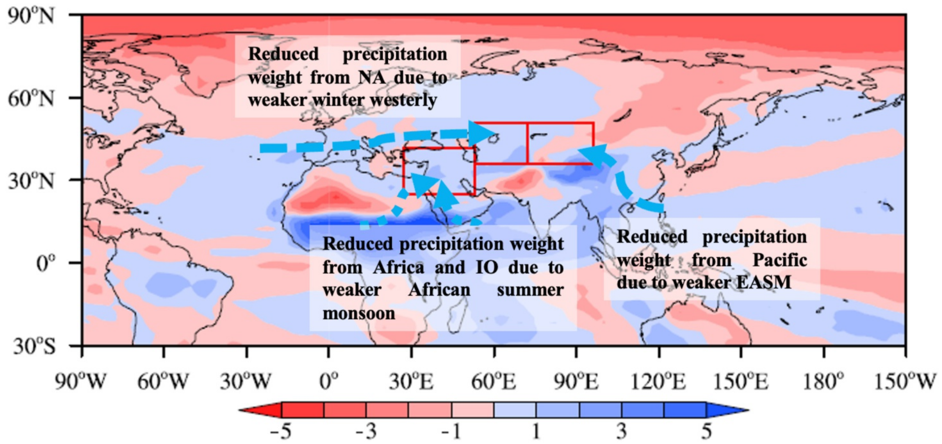

Figure 7. Schematic diagrams illustrating mechanisms behind $\delta^{18}O_p$ changes (unit: ‰) between high precession and low precession over three regions.

Furthermore, these weakened winter polar front westerly jet and strengthened summer subtropical westerly jet, results WA $\delta^{18}O_p$ enrichments due to enriched $\delta^{18}O_p$ sourcing from the North Atlantic through the source and en route effects and reduced precipitation over the North Atlantic Ocean caused by local anti-cyclonic circulation and reduced precipitation along the trajectory. Similar WCA and ECA $\delta^{18}O_p$ enrichments result from $\delta^{18}O_p$ sourcing from the Indian Ocean and Africa through the source and en route effects due to reduced precipitation over the Indian Ocean and Africa caused by African monsoon weakening and reduced precipitation along the trajectory. These circulation changes are mainly induced by the winter polar front westerly jet weakening, summer subtropical westerly jet strengthening, and monsoon weakening due to the precession changes.

The findings from this study inform our understanding of the complex climatic signals contained in speleothem $\delta^{18}O$ records in WA and ACA by providing quantitative estimates of the relative contributions from changes in local precipitation, moisture sources, and water vapor paths. In this case, we find that the shift of moisture source regions dominates the $\delta^{18}O_p$ changes during the Holocene, with a secondary contribution from the $\delta^{18}O_p$ ratio changes within the moisture. Our findings further help resolve the apparent inconsistencies in hydroclimate variations shown in isotope records and other proxy records found in previous studies.

Conflict of Interest

The authors declare no conflicts of interest relevant to this study.

Data Availability Statement

All the simulated results and proxy records used for validation are publicly available for downloading from Zenodo (Ning, Liu, et al., 2025). All the speleothem $\delta^{18}O_c$ records are downloaded from the NOAA Paleoclimatology Data Archive (Comas-Bru et al., 2020). The iTraCE data are downloaded from the Climate Data Gateway at NCAR (Otto-Bliesner et al., 2024). The GNIP $\delta^{18}O_p$ data are downloaded from the GNIP website (ElBaradei, 2025).

Acknowledgments

This research was jointly supported by the National Key Research and Development Program of China (Grant 2023YFF0804700), the Science and Technology Innovation Project of Laoshan Laboratory (No. LSKJ202203300), and the National Natural Science Foundation of China (Grant 42130604, 42575050, 42475051, 42575051, 42111530182, and 42075049).

References

Andrews, J. E., Carolin, S. A., Peckover, E. N., Marca, A., Al-Omari, S., & Rowe, P. J. (2020). Holocene stable isotope record of insolation and rapid climate change in a stalagmite from the Zagros of Iran. *Quaternary Science Reviews*, *241*, 106433. https://doi.org/10.1016/j.quascirev.2020.106433

Chen, F., Jia, J., Chen, J., Li, G., Zhang, X., Xie, H., et al. (2016). A persistent Holocene wetting trend in arid central Asia, with wettest conditions in the late Holocene, revealed by multi-proxy analyses of loess-paleosol sequences in Xinjiang, China. *Quaternary Science Reviews*, *146*, 134–146. https://doi.org/10.1016/j.quascirev.2016.06.002

Chen, F., Xie, T., Yang, Y., Chen, S., Chen, F., Huang, W., & Chen, J. (2023). Discussion of the "warming and wetting" trend and its future variation in the drylands of Northwest China under global warming. *Science China Earth Sciences*, *66*(6), 1241–1257. https://doi.org/10.1007/s11430-022-1098-x

Chen, S., Chen, J., Ding, G., Ma, S., Ji, P., Zhou, A., et al. (2024). Dipole pattern of Holocene hydroclimate variations across the Asian drylands: Critical evidence from West Asia. *J. Geophys. Res. – Atmos*, *129*(7), e2023JD039413. https://doi.org/10.1029/2023JD039413

Chen, S., Chen, J., Lv, F., Liu, X., Huang, W., Wang, T., et al. (2022). Holocene moisture variations in arid central Asia: Reassessment and reconciliation. *Quaternary Science Reviews*, *297*, 107821. https://doi.org/10.1016/j.quascirev.2022.107821

Cheng, H., Sinha, A., Verheyden, S., Nader, F. H., Li, X. L., Zhang, P. Z., et al. (2015). The climate variability in northern Levant over the past 20,000 years. *Geophysical Research Letters*, *42*(20), 8641–8650. https://doi.org/10.1002/2015GL065397

Cheng, H., Spötl, C., Breitenbach, S. F. M., Sinha, A., Wassenburg, J. A., Jochum, K. P., et al. (2016). Climate variations of Central Asia on orbital to millennial timescales. *Scientific Reports*, *5*(1), 36975. https://doi.org/10.1038/srep36975

Cheng, J., Wu, H., Liu, Z., Gu, P., Wang, J., Zhao, C., et al. (2021). Vegetation feedback causes delayed ecosystem response to East Asian Summer Monsoon Rainfall during the Holocene. *Nature Communications*, *12*(1), 1843. https://doi.org/10.1038/s41467-021-22087-2

Comas-Bru, L., Atsawawaranunt, K., & Harrison, S. P., & SISAL working group. (2020). SISALv2: Speleothem Isotopes Synthesis and Analysis database version 2.0 [Dataset]. *NOAA Paleoclimatology Data Archive*. Retrieved from https://www.ncei.noaa.gov/pub/data/paleo/speleothem/SISAL/

Ding, G., Chen, S., Sun, Y., Ma, S., & Chen, J. (2024). Holocene hydroclimatic variations in the Asian drylands: Current understanding and future perspectives. *Journal of Earth Sciences*, *35*(1), 292–295. https://doi.org/10.1007/s12583-023-1958-4

ElBaradei, M. (2025). Global network of isotopes in precipitation (GNIP) ^{18}O data [Dataset]. *Global Network of Isotopes in Precipitation (GNIP) Data Archive*. Retrieved from https://www.iaea.org/services/networks/gnip

Feng, Z., Sun, A., Abdusalih, N., Ran, M., Kurban, A., Lan, B., et al. (2017). Vegetation changes and associated climatic changes in the southern Altai Mountains within China during the Holocene. *The Holocene*, *27*(5), 683–693. https://doi.org/10.1177/0959683616670469

Fleitmann, D., Cheng, H., Badertscher, S., Edwards, R. L., Mudelsee, M., Göktürk, O. M., et al. (2009). Timing and climatic impact of Greenland interstadials recorded in stalagmites from northern Turkey. *Geophysical Research Letters*, *36*(19), L19707. https://doi.org/10.1029/2009GL040050

Göktürk, O. M., Fleitmann, D., Badertscher, S., Cheng, H., Edwards, R. L., Leuenberger, M., et al. (2011). Climate on the southern Black Sea coast during the Holocene: Implications from the Sofular Cave record. *Quaternary Science Reviews*, *30*(19–20), 2433–2445. https://doi.org/10.1016/j.quascirev.2011.05.007

Hao, S., Zhang, X., Duan, Y., Gowan, E. J., Zhu, J., Cauquoin, A., et al. (2025). Model seasonal and proxy spatial biases revealed by assimilated mid-Holocene seasonal temperatures. *Science Bulletin*, *70*, 2014–2022.

He, C., Liu, Z., Otto-Bliesner, B. L., Brady, E. C., Zhu, C., Tomas, R., et al. (2021b). Abrupt Heinrich Stadial 1 cooling missing in Greenland oxygen isotopes. *Science Advances*, *7*(25), eabh1007. https://doi.org/10.1126/sciadv.abh1007

He, C., Liu, Z., Otto-Bliesner, B. L., Brady, E. C., Zhu, C., Tomas, R., et al. (2021a). The hydroclimate footprint accompanying pan-Asian monsoon water isotope evolution during the last deglaciation. *Science Advances*, *7*(4), eabe2611. https://doi.org/10.1126/sciadv.abe2611

Huang, X. Z., Chen, F. H., Fan, Y. X., & Yang, M. L. (2009). Dry late-glacial and early Holocene climate in arid central Asia indicated by lithological and palynological evidence from Bosten Lake, China. *Quaternary International*, *194*(1–2), 19–27. https://doi.org/10.1016/j.quaint.2007.10.002

Jiang, Q., Ji, J., Shen, J., Matsumoto, R., Tong, G., Qian, P., et al. (2013). Holocene vegetational and climatic variation in westerly-dominated areas of Central Asia inferred from the Sayram Lake in northern Xinjiang, China. *Science China Earth Sciences*, *56*(3), 339–353. https://doi.org/10.1007/s11430-012-4550-9

Jing, Z., Liu, Z., Zhang, S., Wen, Q., He, C., Bao, Y., & Yu, W. (2025). Precipitation oxygen isotope variability across timescales in East Asia records two sub-processes of summer monsoon system. *Communications Earth & Environment*, *6*(1), 513. https://doi.org/10.1038/s43247-025-02448-1

Lauterbach, S., Witt, R., Plessen, B., Dulski, P., Prasad, S., Mingram, J., et al. (2014). Climatic imprint of the mid-latitude Westerlies in the Central Tian Shan of Kyrgyzstan and teleconnections to North Atlantic climate variability during the last 6000 years. *The Holocene*, *24*(8), 970–984. https://doi.org/10.1177/0959683614534741

Leroy, S. A. G., López-Merino, L., & Kozina, N. (2019). Dinocyst records from deep cores reveal a reversed salinity gradient in the Caspian Sea at 8.5–4.0 cal ka BP. *Quaternary Science Reviews*, *209*, 1–12. https://doi.org/10.1016/j.quascirev.2019.02.011

Leroy, S. A. G., Kakroodi, A. A., Kroonenberg, S., Lahijani, H. K., Alimohammadian, H., & Nigarov, A. (2013). Holocene vegetation history and sea level changes in the SE corner of the Caspian Sea: Relevance to SW Asia climate. *Quaternary Science Reviews*, *70*, 28–47. https://doi.org/10.1016/j.quascirev.2013.03.004

Li, Y., Song, Y., Kaskaoutis, D. G., Zan, J., Orozbaev, R., Tan, L., & Chen, X. (2021). Aeolian dust dynamics in the Fergana Valley, Central Asia, since∼ 30 ka inferred from loess deposits. *Geoscience Frontiers*, *12*(5), 101180. https://doi.org/10.1016/j.gsf.2021.101180

Liu, X., Liu, J., Shen, C. C., Yang, Y., Chen, J., Chen, S., et al. (2020). Inconsistency between records of δ^{18}O and trace element ratios from stalagmites: Evidence for increasing mid–late Holocene moisture in arid central Asia. *The Holocene*, *30*(3), 369–379. https://doi.org/10.1177/0959683619887431

Liu, X., Rao, Z., Shen, C. C., Liu, J., Chen, J., Chen, S., et al. (2019). Holocene solar activity imprint on Centennial- to multidecadal-scale hydroclimatic oscillations in arid central Asia. *Journal of Geophysical Research: Atmospheres*, *124*(5), 2562–2573. https://doi.org/10.1029/2018JD029699

Liu, Z., Otto-Bliesner, B. L., He, F., Brady, E. C., Tomas, R., Clark, P. U., et al. (2009). Transient simulation of last deglaciation with a new mechanism for Bolling-Allerod warming. *Science*, *325*(5938), 310–314. https://doi.org/10.1126/science.1171041

Ma, S., Chen, S., Chen, J., Chen, J., Cao, D., Xoplaki, E., et al. (2025). The Holocene precipitation dipole pattern in the Asian drylands: Mechanisms and processes from PMIP4 simulations and paleo-proxy evidence. *Quaternary Science Reviews*, *347*, 109091. https://doi.org/10.1016/j.quascirev.2024.109091

Man, W., Zhou, T., Jiang, J., Zuo, M., & Hu, J. (2022). Moisture sources and climatic controls of precipitation stable isotopes over the Tibetan Plateau in water-tagging simulations. *Journal of Geophysical Research: Atmospheres*, *127*(9), e2021JD036321. https://doi.org/10.1029/2021JD036321

Ning, L., Liu, Z., Liu, J., Qin, Y., Xing, F., & Wen, Q. (2025). Data for the paper: "Holocene Hydroclimatic variations over western and central Asia as inferred from stalagmite δ^{18}O evidence" [Dataset]. *Zenodo*. https://doi.org/10.5281/zenodo.17338757

Ning, L., Xing, F., Liu, Z., Liu, J., Mann, M. E., Wu, F., et al. (2025). Tripolar precipitation change accompanying water isotopes in the Holocene reanalysis of Asian monsoon hydroclimate. *Geophysical Research Letters*, *52*(17), e2025GL116451. https://doi.org/10.1029/2025GL116451

Orland, I. J., Bar-Matthews, M., Ayalon, A., Matthews, A., Kozdon, R., Ushikubo, T., & Valley, J. W. (2012). Seasonal resolution of Eastern Mediterranean climate change since 34 ka from a Soreq Cave speleothem. *Geochimica et Cosmochimica Acta*, *89*, 240–255. https://doi.org/10.1016/j.gca.2012.04.035

Orland, I. J., He, F., Bar-Matthews, M., Chen, G., Ayalon, A., & Kutzbach, J. E. (2019). Resolving seasonal rainfall changes in the Middle East during the last interglacial period. *Proceedings of the National Academy of Sciences*, *116*(50), 24985–24990. https://doi.org/10.1073/pnas.1903139116

Otto-Bliesner, B., Tomas, E. B. R., Liu, Z., & He, C. (2024). iTraCE [Dataset]. *Research Data Archive at the National Center for Atmospheric Research, Computational and Information Systems Laboratory*. https://doi.org/10.26024/b290-an76

Sharifi, A., Ali, P., Canuel, E. A., Ferer-Tyler, E., Peterson, L. C., Aichner, B., et al. (2015). Abrupt climate variability since the last deglaciation based on a high-resolution, multi-proxy peat record from NW Iran: The hand that rocked the Cradle of Civilization? *Quaternary Science Reviews*, *123*, 215–230. https://doi.org/10.1016/j.quascirev.2015.07.006

Tan, L., Cheng, H., Li, D., Orozbaev, R., Li, Y., Xu, H., et al. (2024). Hydroclimatic changes on multiple timescales since 7800 y BP in the winter precipitation-dominated Central Asia. *Proc. Nat. Acad. Sci. USA*, *121*(14), e2321645121. https://doi.org/10.1073/pnas.2321645121

Wang, W., & Feng, Z. (2013). Holocene moisture evolution across the Mongolian Plateau and its surrounding areas: A synthesis of climatic records. *Earth-Science Reviews*, *122*, 38–57. https://doi.org/10.1016/j.earscirev.2013.03.005

Wen, Q., Liu, Z., Liu, J., Clemens, S., Jing, Z., Wang, Y., et al. (2024). Contrasting responses of Indian summer monsoon rainfall and Arabian Sea upwelling to orbital forcing. *Communications Earth & Environment*, *5*(1), 409. https://doi.org/10.1038/s43247-024-01572-8

Wick, L., Lemcke, G., & Sturm, M. (2003). Evidence of Lateglacial and Holocene climatic change and human impact in eastern Anatolia: High-resolution pollen, charcoal, isotopic and geochemical records from the laminated sediments of Lake Van, Turkey. *The Holocene*, *13*(5), 665–675. https://doi.org/10.1191/0959683603hl653rp

Zhang, Y., Meyers, P. A., Liu, X., Wang, G., Ma, X., Li, X., et al. (2016). Holocene climate changes in the central Asia mountain region inferred from a peat sequence from the Altai Mountains, Xinjiang, northwestern China. *Quaternary Science Reviews*, *152*, 19–30. https://doi.org/10.1016/j.quascirev.2016.09.016